Journal of Solid State Chemistry **159,** 121–129 (2001)
doi:10.1006/jssc.2001.9139, available online at http://www.idealibrary.com on IDEAL®

The Strain-Driven Pyrochlore to "Defect Fluorite" Phase Transition in Rare Earth Sesquioxide Stabilized Cubic Zirconias

Y. Tabira,* R. L. Withers,*,[1] J. C. Barry,† and L. Elcoro‡

*Research School of Chemistry, Australian National University, Canberra, A.C.T. 0200, Australia; †Centre for Microscopy and Microanalysis, University of Queensland, St. Lucia, Queensland, Australia; and ‡Departamento de Fisica de la Materia Condensada, Universidad del Pais Vasco, Bilbao, E-48080, Spain

Received November 2, 2000; in revised form February 26, 2001; accepted March 5, 2001; published online May 14, 2001

The relationship between the ordering characteristic of the pyrochlore structure type and that characteristic of the "defect fluorite" structure type (immediately on either side of two phase regions separating the two structure types) in a range of rare eath sesquioxide stabilized cubic zirconias is investigated via electron diffraction and imaging. Systematic structural change as a function of composition and relative size of the constituent metal ions is highlighted and a multi-q to single-q = 1/2 [111]* model proposed for the observed pyrochlore to defect fluorite phase transition. Strain introduced into the close-packed {111} metal ion planes of the defect fluorite average structure by the local cation and oxygen vacancy distribution is pointed to as the likely origin of the observed behavior. © 2001 Academic Press

1. INTRODUCTION

The crystal symmetry of ZrO_2 is monoclinic up to $\sim$1170°C, tetragonal between $\sim$1170° and 2370°C, and cubic (fluorite type) from $\sim$2370°C up to the melting point at $\sim$2830°C (1). The latter, nonquenchable, cubic form of zirconia can, however, be "stabilized" to room temperature via the addition of greater than $\sim$10–20 mol% of lower valent metal oxides (such as CaO, MgO, or the rare earth (lanthanide) sesquioxides) followed by subsequent quenching from a sufficiently elevated temperature ($\sim$1400°–1600°C) (1–3). The resultant cubic stabilized zirconia (CSZ) solid solutions typically exist over a very wide composition range (1–3) with an average "defect fluorite" type structure (see Fig. 1).

Density measurements show that the fcc metal atom sites therein (corresponding to the vertices of the tetrahedra in Fig. 1) are always fully occupied but that vacancies necessarily occur in the oxygen sublattice (the sites at the centers of the tetrahedra in Fig. 1). The presence of these vacancies and the associated mobility of the remaining oxygen anions at temperatures above $\sim$700°C give such anion-deficient defect fluorite materials important oxygen ion conductivity properties leading to applications such as, for example, their use as components in solid oxide fuel cells (4).

The focus of this paper is the rare earth sesquioxide stabilized CSZ's. For the lighter rare earth elements (from Ln = La to Gd), a typical "phase diagram" of these anion-deficient $(1-x)ZrO_2.xLnO_{1.5}$ systems (obtained by analysis of specimens quenched from $\sim$1500 to 1600°C) as a function of increasing $LnO_{1.5}$ concentration (1, 2, 5–7) shows an initial tetragonal (T) solid solution region (up to $\sim$5 mol%) giving way (via two phase regions) first to a defect fluorite (df) solid solution region which in turn gives way to a pyrochlore (P) solid solution region (centered around $\sim$50 mol% $LnO_{1.5}$, but with a strongly lanthanide size-dependent composition width) followed by a return to a defect fluorite region before a final transition to either an A or B-type sesquioxide region at very high (>90 mol%) $LnO_{1.5}$ concentrations (see Fig. 2). While the A- and B-type sesquioxide structure types are not fluorite related, the pyrochlore structure type is and can be described as a modulated variant thereof. In the case of the heavier rare earth elements beyond Gd, the pyrochlore structure type is no longer found. Instead, the defect fluorite solid solution region is extended up to $\sim$75 mol% $LnO_{1.5}$ beyond which a transition to either the B- or C-type sesquioxide structure type takes place. The former is not a fluorite-related structure type while the latter is.

In those cases where a pyrochlore solid solution phase does occur, there is usually a high temperature phase transition from pyrochlore to the defect fluorite phase before melting. The temperature of this phase transition is lowest for Ln = Gd ($\sim$1530°C) and increases systematically with Ln size until Ln = La where the phase transition no longer takes place and the pyrochlore phase is stable all the way up to the melting point. The extent of the pyrochlore solid solution region has recently been found to be strongly Ln size dependent (5–7) with a lowest composition width

[1] To whom correspondence should be addressed.

0022-4596/01 $35.00

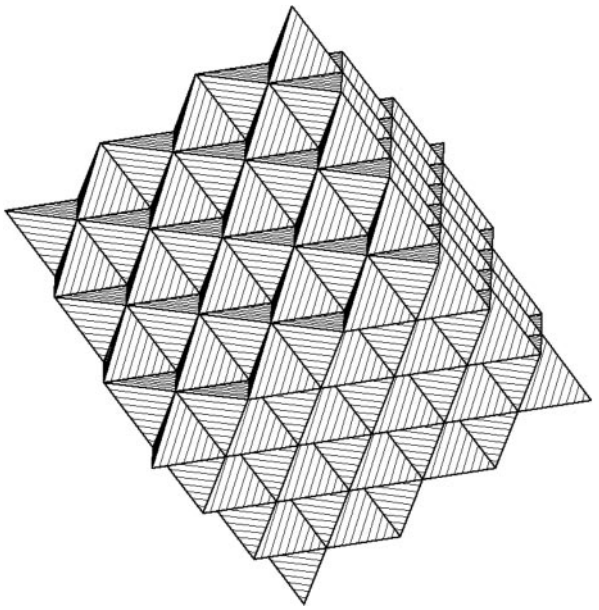

FIG. 1. The defect fluorite average structure of $(1-x)ZrO_2 . xLnO_{1.5}$ CSZ's shown tilted slightly away from a $\langle 110 \rangle$ projection. The representation shown uses oxygen-centered OM_4 tetrahedra with the fcc metal ion array (M = Zr, Ln) occupying the corners of these tetrahedra.

($< \sim 2$ mol% width at 1500°C) for Ln = La (5), which increases systematically with reducing Ln size (~ 17 mol% for Ln = Sm at 1500°C) (6).

Oxygen mobility and hence ionic conductivity is known to be strongly affected by this pyrochlore to defect fluorite phase transition as well as by aging and dopant concentration within both the defect fluorite and pyrochlore solid solution fields (8–13). This suggests the importance of ordering and associated structural relaxation and spurred the initial structural investigation of these materials (14–17). As well as the strong Bragg reflections of the underlying defect fluorite type average structure, labelled **G** in what follows, it was rapidly discovered that the reciprocal lattices of these cubic stabilized zirconias (CSZ's) invariably contained additional, composition-dependent (and often highly structured) diffuse scattering (14–26; see also (4) and references contained therein).

Despite numerous investigations over a long period of time into the implied metal ion and oxygen vacancy ordering patterns and accompanying structural relaxation) associated with this additional diffuse scattering, significant consensus is still far from being reached (2, 4, 7–8, 12–27). One approach interprets observed diffuse intensity in terms of small microdomains of ordered fluorite-related superstructure phases embedded within an undistorted fluorite type matrix (15, 20–22). Another emphasizes short-range local order and hence tends to use the language of short-range order parameters (18, 25, 26) while a third (in the case where the observed diffuse distribution appears to be closely related to the pyrochlore structure type — see below) emphasizes the importance of antiphase boundaries separating pyrochlore microdomain regions (14, 20, 24, 27). A final approach uses the language of modulated structures (4, 7, 26). Some or all of these various approaches have been discussed in (4, 13).

The focus of this paper is the relationship between the ordering characteristic of the pyrochlore structure type and that characteristic of the defect fluorite structure type immediately on either side of the two phase regions separating the two structure types (see Fig. 2) as well as the dependence of this ordering upon the relative sizes of the Ln^{3+} and Zr^{4+}

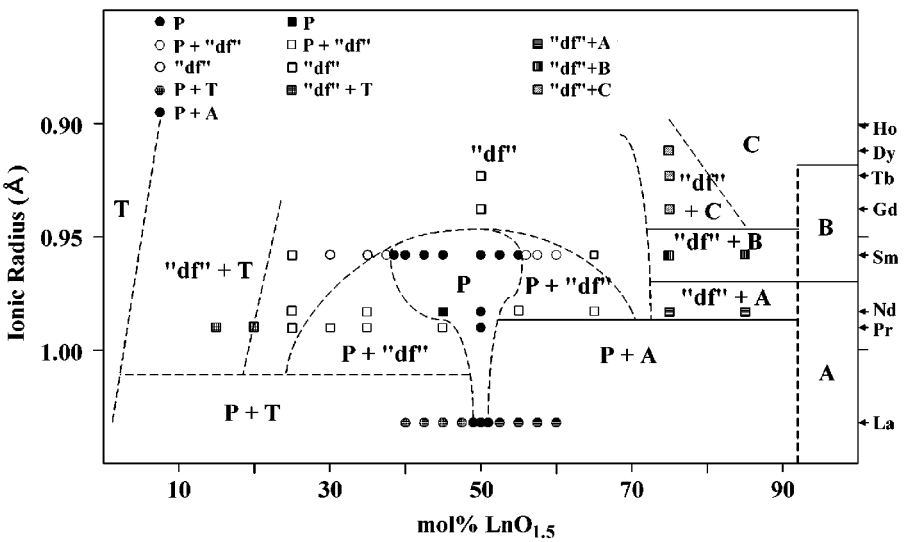

FIG. 2. Summary of the phase relationships of $(1-x)ZrO_2.xLnO_{1.5}$ systems quenched from high temperatures ($\sim$1500–1600°C) as a function of lanthanide ionic radii (taken from Table 1 of Ref. (32)). The data points represented by the various symbols are largely taken from Refs. (6, 7, 22).

TABLE 1

Ideal d(O–M) Bond Length within a Hypothetical OM_4 tetrahedra (See Fig. 1), for a Range of Rare Earth and Other Cations M, Calculated Using the Bond Valence Parameters (R_0's) Given by Brese and O'Keeffe (33)

Ion M	$R_0(O^{2-}–M)$	$d(O^{2-}–M)$	$d(M–M)$
La^{3+}	2.172	2.428	3.965
Pr^{3+}	2.135	2.391	3.904
Nd^{3+}	2.117	2.373	3.875
Sm^{3+}	2.088	2.344	3.828
Gd^{3+}	2.065	2.321	3.790
Tb^{3+}	2.049	2.305	3.764
Dy^{3+}	2.036	2.292	3.743
Ho^{3+}	2.023	2.279	3.722
Y^{3+}	2.014	2.270	3.707
Ca^{2+}	1.967	2.223	3.630
Zr^{4+}	1.937	2.196	3.586

Note. The corresponding ideal $d(M–M)$ tetrahedral edge lengths are also listed to give some indication of the local strain introduced into the close-packed $\{111\}$ metal ion planes of the defect fluorite average structure by the local cation distribution.

ions (1, 2). Rare earth sesquioxide stabilized cubic zirconia systems provide a very useful family of materials within which to investigate such systematic change as a result of the ability to virtually continuously vary the relative size of the constituent Ln and Zr metal ions and hence the local strain in the "defect fluorite" average structure (see, for example, Table 1).

The pyrochlore structure type is characterized in real space by correlated $\{111\}$ metal ion and oxygen vacancy ordering and (in reciprocal space) by the presence of sharp $\mathbf{G} \pm \frac{1}{2}\langle 111\rangle^*$ type satellite reflections (where $\mathbf{G}$ corresponds to the strong Bragg reflections of the underlying defect fluorite type average structure). We therefore focus on those regions of the $(1-x)ZrO_2.xLnO_{1.5}$ defect fluorite solid solutions where strong diffuse intensity is likewise localized near $\mathbf{G} \pm \frac{1}{2}\langle 111\rangle^*$ regions of reciprocal space (primarily those regions immediately surrounding the two phase regions separating pyrochlore and defect fluorite phase fields; see Fig. 2).

2. EXPERIMENTAL

The synthesis of the $(1-x)ZrO_2.xLnO_{1.5}$ specimens used in this study is described in Refs. (5–7, 22). Electron microscope samples were prepared by crushing and dispersing onto holey carbon-coated copper grids, which were subsequently examined in JEOL 100CX, JEOL 4010, and Philips EM430 Transmission Electron Microscopes (TEM's). The high-resolution transmission electron microscope (HRTEM) images were obtained using a JEOL 4010 TEM ($C_s = 0.7$ mm; structure resolution limit = 1.4 Å) operating at 400 kV. The HRTEM images were captured on Kodak SO-163 electron image film, and these images were subsequently digitized using a LeafScan 45 negative scanner.

3. RESULTS

That the metal ion and oxygen vacancy ordering characteristic of the pyrochlore structure type also exists on the defect fluorite side of the two phase regions separating the two structure types is apparent from the $\langle 110\rangle_F$ (F for fluorite) zone axis Electron Diffraction Patterns (EDP's) shown in Fig. 3. The first three EDP's are from (a) a 25 mol% $PrO_{1.5}$ specimen, (b) a 35 mol% $SmO_{1.5}$ specimen, and (c) a 50 mol% $GdO_{1.5}$ specimen (quenched from above the pyrochlore to defect fluorite phase transition at $\sim$1530°C). These first three materials are all in defect fluorite regions of their respective phase diagrams (see Fig. 2) although with quite different compositions. The EDP shown in Fig. 3d, by contrast, is from a 50 mol% $LaO_{1.5}$ specimen and is representative of the pyrochlore structure type itself with sharp satellite reflections at all $\mathbf{G} \pm \frac{1}{2}\langle 111\rangle^*$ positions of reciprocal space.

Additional scattering is also present in each of the first three EDP's at, or very close to, the same positions of reciprocal space, i.e., at the $\mathbf{G} \pm \frac{1}{2}\langle 111\rangle^*$ regions of reciprocal space. Such intense $\mathbf{G} \pm \sim \frac{1}{2}\langle 111\rangle^*$ type "diffuse scattering" is characteristic of all defect fluorite CSZ's for regions of the relevant phase diagram immediately surrounding the corresponding P + df two phase regions (see Fig. 2). It definitely does not only occur for compositions near the nominal ideal pyrochlore composition of 50 mol% $LnO_{1.5}$. (A rather similar EDP to those shown in Figs. 3a–3c has also recently been published for an $\sim$ 62 mol% $SmO_{1.5}$ defect fluorite specimen (see Fig. 3c of (6)). This composition is still very close to the P + df two-phase region (see Fig. 2) but now on the other side of the pyrochlore phase region to the 35 mol% $SmO_{1.5}$ specimen. Intense $\mathbf{G} \pm \sim \frac{1}{2}\langle 111\rangle^*$ type diffuse scattering, however, still occurs.)

Note furthermore the systematic change in the sharpness and shape of the $\mathbf{G} \pm \sim \frac{1}{2}\langle 111\rangle^*$ type "satellite reflections" (fairly sharp in the case of (a), slightly smeared out in (b), and even more smeared out in (c)) as a function of Ln ion size ($Pr^{3+} > Sm^{3+} > Gd^{3+}$) and the fact that the smearing is largely perpendicular to the local $\langle 111\rangle^*$ reciprocal space direction. Clearly the metal ion and oxygen vacancy ordering pattern responsible has a fairly long correlation length along the corresponding $\langle 111\rangle$ real space direction but a rather shorter correlation length in the orthogonal $\{111\}$ plane, particularly in the case of the 50 mol% $GdO_{1.5}$ specimen.

To emphasize further the systematic nature of the structural changes occurring as a function of deviation from the relevant P + df two phase region (by, for example, varying Ln^{3+} ion size at a fixed composition in stabilized zirconia

systems), consider the $\langle 110\rangle_F$ and $\langle 112\rangle_F$ zone axis EDP's of the 50 mol% $TbO_{1.5}$ specimen shown in Fig. 4. Instead of additional scattering smeared about the $\mathbf{G} \pm \frac{1}{2}\langle 111\rangle^*$ positions of reciprocal space as for the 50 mol% $GdO_{1.5}$ specimen, fairly sharp diffuse rings of intensity surrounding the $\mathbf{G} \pm \frac{1}{2}\langle 111\rangle^*$ positions of reciprocal space now occur (9, 24, 26). Intriguingly, this fundamental change in character of the additional intense diffuse scattering correlates with the disappearance of the pyrochlore structure type itself from equilibrium phase diagrams, at least for compositions close to 50 mol% $LnO_{1.5}$ (see Fig. 2).

Such strong "smoke ring like" diffuse scattering is also characteristic of a range of other stabilized zirconia systems ($Zr_{0.61}Y_{0.39}O_{1.805}$ and $Zr_{0.875}Ca_{0.125}O_{1.875}$ (26), for example) as well as of other related defect fluorite type phases (4, 27). For all such systems exhibiting smoke ring like diffuse scattering, however, just as for the $(1-x)$ $ZrO_2.xTbO_{1.5}$ system, there is no longer a stable pyrochlore phase in the relevant phase diagram; *i.e.*, when the size difference of the dopant cation from Zr^{4+} becomes too small (see Table 1) then the pyrochlore structure type itself is destabilized. Clearly, strain induced by the local metal ion distribution (see Table 1) plays an important role in determining the form of the phase diagram (see Fig. 2).

It is known that the radii of these diffuse circles around $\frac{1}{2}\langle 111\rangle^*$ differ for different stabilized zirconia systems and furthermore correlate strongly with the difference in size of the constituent metal ions (24). Indeed, Miida *et al.* (24) have proposed that the diffuse rings arise from a distribution of antiphase boundaries (APB's) in (111) planes whose role is to reduce the accumulation of local strain arising as a result of metal ion ordering along the orthogonal [111] direction.

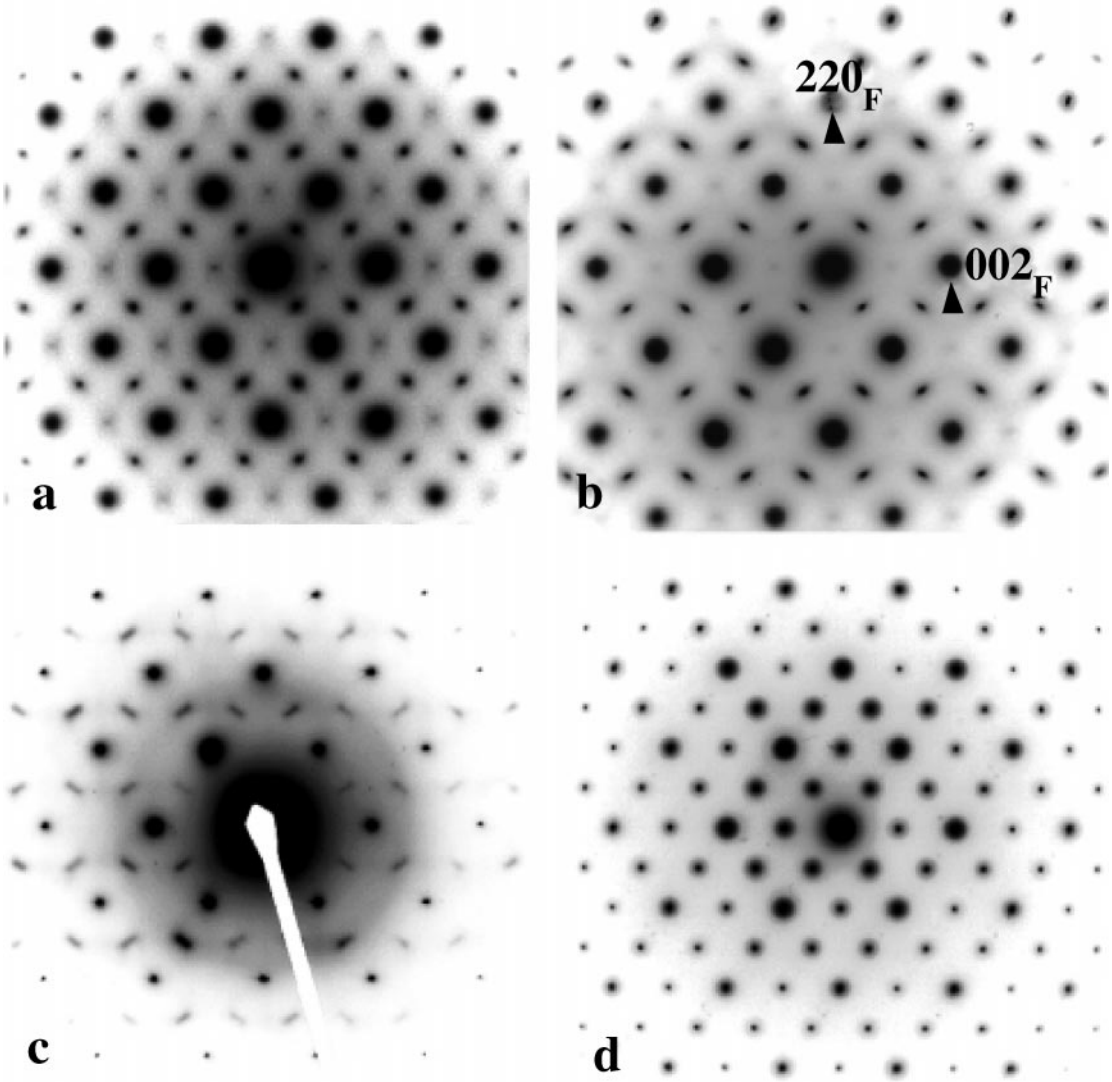

FIG. 3. $\langle 110\rangle$ zone axis electron diffraction patterns (EDP's) typical of (a) 25 mol% $PrO_{1.5}$, (b) 35 mol% $SmO_{1.5}$, (c) 50 mol% $GdO_{1.5}$ (quenched from above the pyrochlore to defect fluorite phase transition in this system) and (d) 50 mol% $LaO_{1.5}$ specimens, respectively.

They propose that the separation of these APB's in the (111) planes determines the ring radius and is directly related to the difference in size of the host and guest cations. A similar suggestion that the smoke ring like diffuse arises as a result of a compromise between local attractive forces trying to force pyrochlore-like ordering and longer range strain forces constraining the lateral extent of any such ordering has also recently been proposed by Welberry (28).

It would seem that strain associated with the essentially close-packed metal ion sublattice (mediated by the Ln^{3+}/Zr^{4+} metal ion distribution itself as well as the underlying oxygen vacancy distribution) is playing a crucial role and that the distribution of metal ions and oxygen vacancies should be such as to minimize the resultant strain in the metal ion sublattice, particularly in the close-packed $\{111\}$ metal ion planes.

To a first approximation, the various $\langle 110\rangle_F$ EDP's shown in Fig. 3 are all quite similar. There are, however, significant differences between the EDP's characteristic of the defect fluorite phase immediately surrounding the relevant P + df two phase regions and those characteristic of the pyrochlore structure type. In addition to the somewhat smeared nature of the primary $\mathbf{G} \pm \frac{1}{2}\langle 111\rangle^*$ "satellite reflections," the second harmonic $\mathbf{G} \pm \langle 001\rangle^*$ type satellite reflections are always much weaker if not altogether absent on the defect fluorite side of the two-phase region, whereas the same reflections are clearly present in the pyrochlore phase field. This is most apparent by comparison of defect fluorite and pyrochlore type $\langle 001\rangle_F$ zone axis EDP's (cf., for example, the $\langle 001\rangle_F$ EDP's of (a) a 35 mol% $SmO_{1.5}$ defect fluorite specimen and (b) a 50 mol% $SmO_{1.5}$ pyrochlore specimen shown in Fig. 5).

The clear change in the relative intensities of the second harmonic $\mathbf{G} \pm \langle 001\rangle^*$ type satellite reflections to those of the primary $\mathbf{G} \pm \frac{1}{2}\langle 111\rangle^*$ satellite reflections is incompatible with the suggestion that the existence of $\mathbf{G} \pm \frac{1}{2}\langle 111\rangle^*$ satellite reflections on the defect fluorite side of the two-phase region could be due to a diphasic texture of pyrochlore type microdomains embedded coherently within a fluorite matrix (20). Note that such a (nonequilibrium) diphasic interpretation would also be incompatible with the quite reproducible existence of two phase regions separating the two distinct structure types (5–7, 22).

The question becomes what is the exact nature of the structural similarities and differences between the two solid solution fields? We believe the virtual absence of second harmonic $\mathbf{G} \pm \langle 001\rangle^*$ type satellite reflections provides an important clue. In the case of potential multi-**q** modulated systems, the absence of higher order harmonic satellite reflections is often taken as a good indication of a single-**q** state; i.e., it implies that only one of the initially symmetry-equivalent primary modulation wave-vectors exist in any one local region. In the current context, that would imply that only one of the four initially symmetry-equivalent $\frac{1}{2}\langle 111\rangle^*$ type modulation waves is present in any one local region.

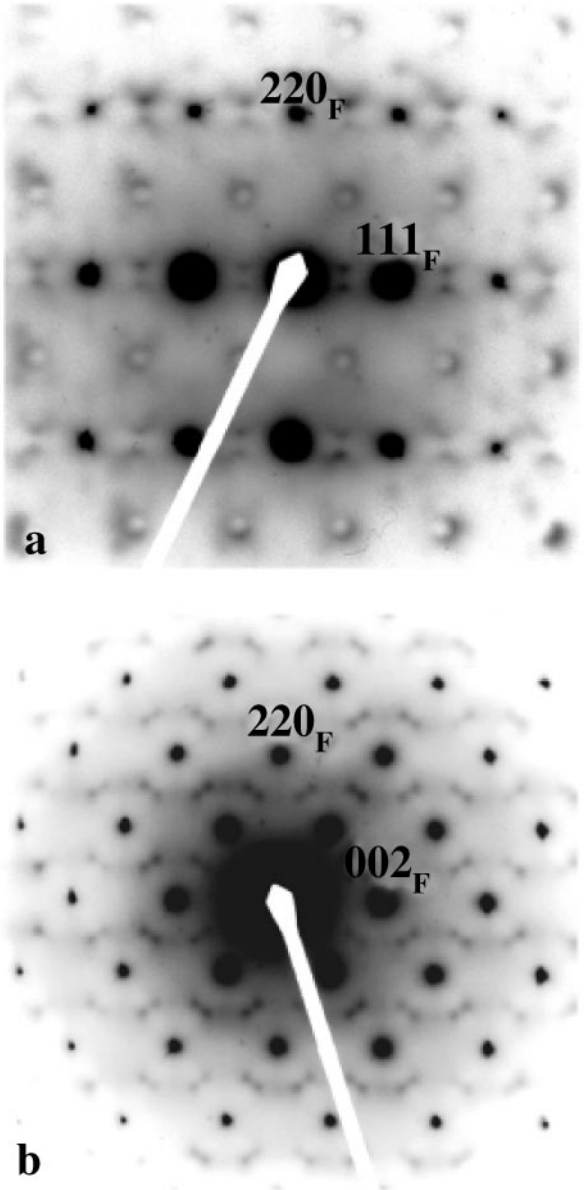

FIG. 4. Typical $\langle 110\rangle$ and $\langle 112\rangle$ zone axis EDP's for a 50 mol% $TbO_{1.5}$ specimen.

An individual $\mathbf{q} = \frac{1}{2}\langle 111\rangle^*$ modulation in the case of the pyrochlore structure type is necessarily associated with correlated metal ion and oxygen vacancy ordering and associated structural relaxation (as schematically shown in, for example, Fig. 6 of (7)). Experimentally, for example, the reciprocal space intensity distribution of the $\mathbf{G} \pm \frac{1}{2}\langle 111\rangle^*$ satellite reflections in the case of the defect fluorite phase regions is rather similar to that in the pyrochlore phase field (see Fig. 3) requiring that a similar ordering pattern must also hold on the defect fluorite side of the two-phase region;

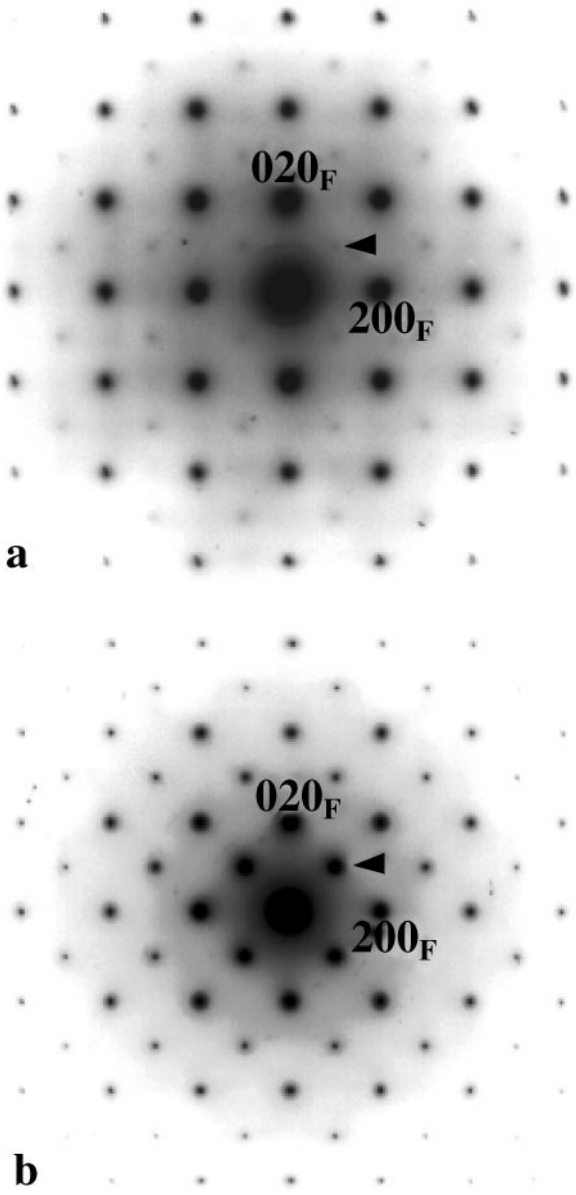

FIG. 5. $\langle 001 \rangle$ zone axis EDP's for an (a) 35 mol% $SmO_{1.5}$ specimen and (b) a 50 mol% $SmO_{1.5}$ specimen. The former is typical of the defect fluorite phase immediately surrounding the relevant P + df two phase regions while the latter is characteristic of the pyrochlore phase field. Note the virtual absence of second harmonic $\mathbf{G} \pm \langle 001 \rangle^*$ type satellite reflections in (a).

i.e., the compositional and displacement eigenvectors (7) associated with an individual $\frac{1}{2}\langle 111 \rangle^*$ modulation wave are essentially the same on either side of the two-phase region and cannot be held responsible for the phase transition. An explanation must be sought elsewhere. If differences in the compositional and displacement eigenvectors associated with individual $\frac{1}{2}\langle 111 \rangle^*$ modulation waves are not the origin of the phase transition, then it must be the correlation between the four possible such modulation waves that is responsible.

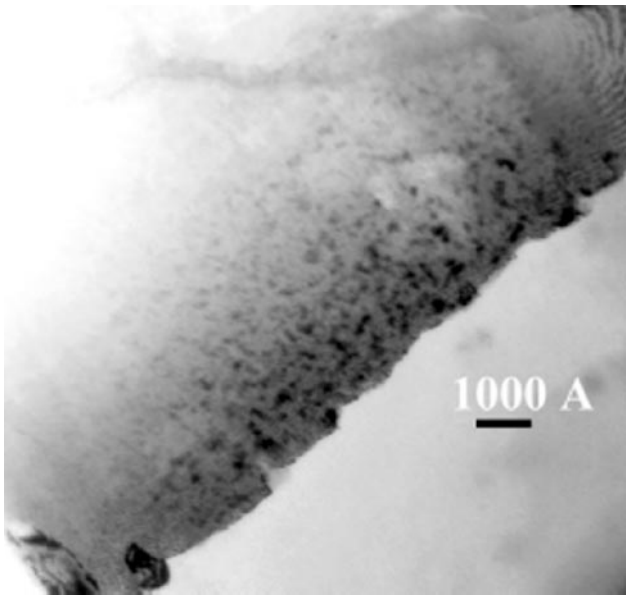

FIG. 6. A typical satellite dark field (SDF) image of the 25 mol% $PrO_{1.5}$ specimen taken using a $\mathbf{G} \pm \frac{1}{2}[111]^*$ satellite reflection. A microdomain structure on the 100–200 Å scale is readily apparent.

The cubic *Fd3m* space group symmetry of the pyrochlore structure type not only determines the compositional and displacement eigenvectors associated with an individual $\frac{1}{2}\langle 111 \rangle^*$ modulation wave but also ties together the amplitudes and phases of the four distinct $\mathbf{q} = \frac{1}{2}\langle 111 \rangle^*$ modulation waves (see, for example, Eq. (12) of (7)). (It is this tying together of the four distinct constituent $\mathbf{q} = \frac{1}{2}\langle 111 \rangle^*$ compositional modulation waves that gives rise to what Nyman *et al.* (29) have refererred to as the "essential pyrochlore unit," i.e., the characteristic tetrahedra of Zr_4 metal ions (or tetrahedra of ZrO_6 octahedra) which arises when the individual $\frac{1}{2}\langle 111 \rangle^*$ compositional modulation waves intersect).

Satellite dark field images within the pyrochlore solid solution field using individual $\mathbf{G} \pm \frac{1}{2}\langle 111 \rangle^*$ type satellite reflections thus show no evidence for microdomains. Such is not the case, however, on the defect fluorite side of the two-phase region. Figure 6, for example, shows a typical such satellite dark field (SDF) image (albeit at low resolution) for the 25 mol% $PrO_{1.5}$ specimen. (Similar SDF images have also been obtained for the 35 mol% $SmO_{1.5}$ specimen.) A microdomain texture on the 100–200 Å scale is readily apparent. The dark regions in this image correspond to regions where the amplitude of the corresponding $\frac{1}{2}\langle 111 \rangle^*$ modulation wave is necessarily zero and show that there is a fundamental change in local symmetry on moving to the defect fluorite side of the two-phase region. (Note that such contrast cannot be interpreted in terms of antiphase boundaries (20).)

This is confirmed by the $\langle 110 \rangle_F$ HREM image shown in Fig. 7a and, more particularly, by the corresponding image

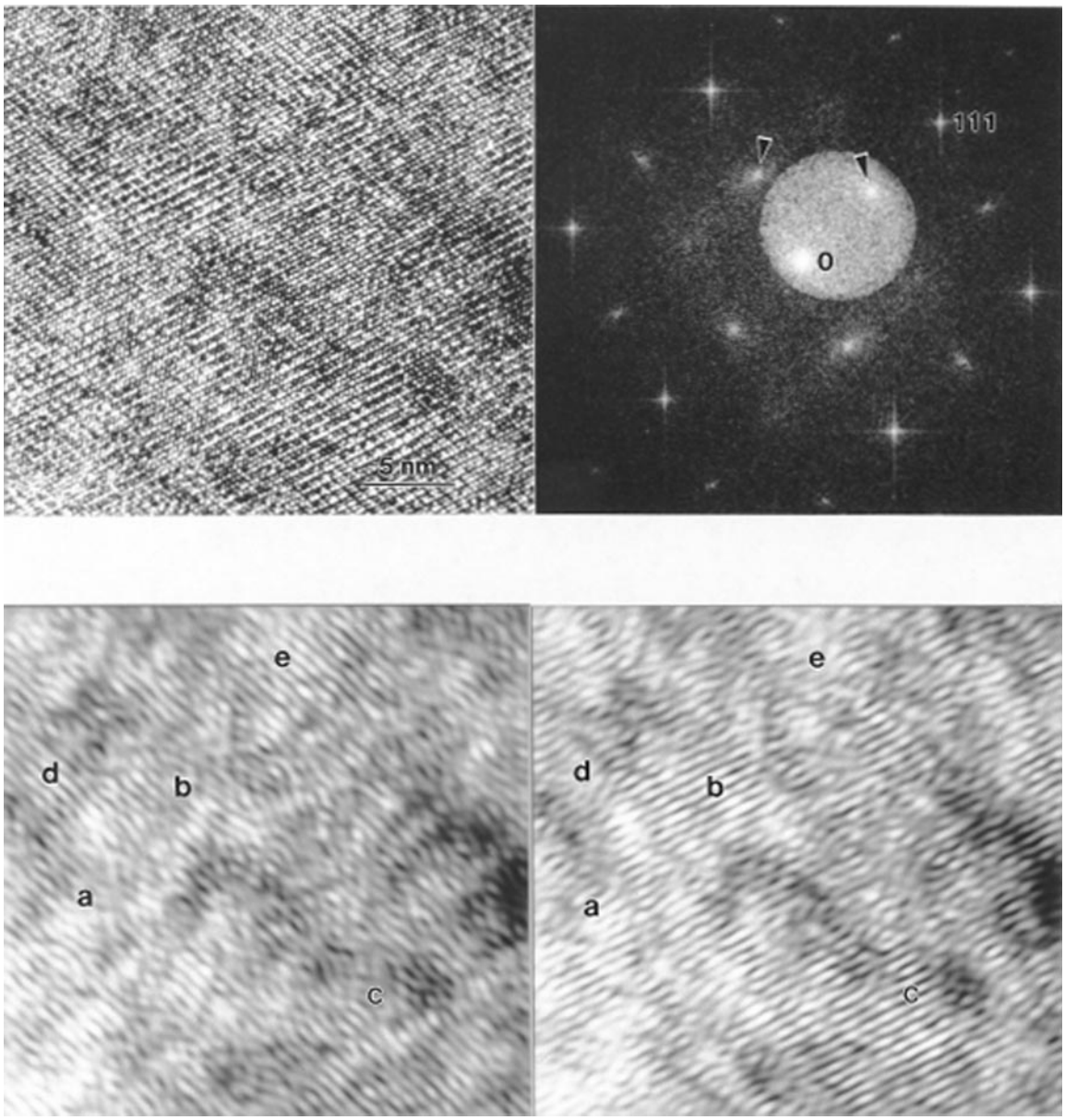

FIG. 7. (a) A typical $\langle 110 \rangle_F$ HREM image of the 25 mol% $PrO_{1.5}$ specimen. (b) A power spectrum obtained by Fourier transformation of the image in (a). The two $\frac{1}{2}\langle 111 \rangle^*$ satellite reflections are arrowed and the center of the pattern labeled "0." The size and position of the Fourier mask used to obtain (c) can be seen highlighted in (b). (c) The processed image using the Fourier mask highlighted in (b). (d) The processed image using the central beam and the alternative $\frac{1}{2}\langle 111 \rangle^*$ satellite reflection. Identical positions are marked with the letters *a* to *e* in (c) and (d).

processed SDF images shown in Figs. 7c and 7d and obtained from Fig. 7a via fourier filtering as indicated in Fig. 7b. The specimen thickness in the area (as judged by the appearance of the lattice image) is between 100 and 300 Å while the defocus is close to scherzer (optimum) defocus. Each SDF image is obtained by selecting the central beam and one of the two $\frac{1}{2}\langle 111 \rangle^*$ satellite reflections arrowed in Fig. 7b. The visibility of the $2a_F/\sqrt{3} \sim 6$ Å fringes corresponding to the doubling of the average defect fluorite periodicity along the particular [111]* direction chosen by the fourier masks is clearly quite inhomogeneous in Figs. 7c and 7d and there are many regions where one or other of these sets of fringes exist but not the other. In Fig. 7d, for example, there exist fringes at points *a*, *b*, and *c* whereas there are no fringes at these points in Fig. 7c. Likewise, in Fig. 7c there exist fringes at points *d* and *e* but there are no fringes at these points in Fig. 7d. These results are compatible with the low-resolution SDF image of Fig. 6 and suggest that there are domains of 100–150 Å in size where only one of the four potential $\frac{1}{2}\langle 111 \rangle^*$ modulation waves is locally present.

However, given that only two of the four potential $\frac{1}{2}\langle 111\rangle^*$ modulation waves can ever be excited in any one such $\langle 110\rangle_F$ image and the fact that the boundary regions separating these microdomain regions do not run along any sort of crystallographic direction (so that it is never clear in such images whether one is projecting through one or, more likely, several such domains), it is not of course strictly possible to prove the existence of a local single-**q** state from such images. Nonetheless, there is undoubtedly a clear change of symmetry from the pyrochlore to the defect fluorite side of the two-phase region in this system and the most likely explanation is a multi-**q** (cubic) to single-**q** (rhombohedral) phase transition.

It is interesting at this point to note that there exist various modulated phases (not normally thought of as being pyrochlore related phases), which also possess an average fluorite-type structure and are likewise characterized by metal ion ordering in $\{111\}$ planes. Examples include the $(1-x)Bi_2O_3.xNb_2O_5$, $0.06 < x < 0.23$, type II solid solution phase (30) as well as the $CaUO_4$ phase (31). In the case of the $(1-x)Bi_2O_3.xNb_2O_5$, $0.06 < x < 0.23$, type II solid solution phase, for example, the average structure is of defect fluorite type and the (primitive) primary modulation wave vectors again run along $\langle 111\rangle^*$ directions but this time the magnitude is not $\frac{1}{2}\langle 111\rangle^*$ but rather $\varepsilon\langle 111\rangle^*$ with $\varepsilon \sim 0.37$ (30). Nevertheless the same phase relationship between the four $\mathbf{q} = \varepsilon\langle 111\rangle^*$ compositional modulation waves as is characteristic of the pyrochlore structure type is also characteristic of this three-dimensional incommensurately modulated cubic phase. On the other hand, $CaUO_4$ can be described rather more simply as a rhombohedral, single-$\mathbf{q} = \frac{1}{2}$ [111]* modulated fluorite phase (see Fig. 7 of (7)) of the type proposed here for the df side of the P + df two phase region.

4. DISCUSSION AND CONCLUSIONS

The systematic changes in phase relationships, occasioned either by variation in composition or by a variation in the relative sizes of the Zr^{4+} and Ln^{3+} ions at the same composition, within these anion-deficient $(1-x)ZrO_2.xLnO_{1.5}$ systems (and highlighted in the current contribution) are important and need to be understood in local crystal chemical terms. While such an ambitious aim is beyond the scope of the current contribution, there are nonetheless important conclusions that can be drawn from the observed behavior. In particular, it seems clear that strain associated with the essentially close packed metal ion $\{111\}$ planes (mediated by the metal ion distribution itself (see Table 1) as well as by the underlying oxygen vacancy distribution) is playing a crucial role and that the distribution of metal ions and oxygen vacancies are usually such as to minimize the resultant strain in these $\{111\}$ metal ion planes.

For satellite reflections to be localized close to the $\mathbf{G} \pm \frac{1}{2}\langle 111\rangle^*$ positions of reciprocal space, strain must be matched for alternate $\{111\}$ metal ion planes. This will depend upon the balance between the concentration and distribution of oxygen vacancies and metal ions (see Table 1). The fact that the pyrochlore structure type exists only when the size difference between the rare earth Ln^{3+} ion and Zr^{4+} is large requires that oxygen vacancies must be preferentially associated with the smaller Zr^{4+} ion (and hence with alternate $\{111\}$ metal ion planes) in order to compensate for the metal ion size difference (see Table 1).

When the metal ion size difference is largest (for Ln = La), the compositional width of the pyrochlore solid solution field is narrowest. As this metal ion size difference decreases, the compositional width of the pyrochlore solid solution field systematically increases; i.e., the metal ion distribution of the ideal pyrochlore structure type becomes more and more flexible with Zr^{4+} ions becoming able to replace Ln^{3+} ions and vice-versa. Simultaneously, the compositional width of the surrounding df phase field increases. Eventually, when the metal ion size difference becomes too small, the pyrochlore phase itself is destabilized altogether and a phase transition to a single-$\mathbf{q} = \frac{1}{2}[111]^*$ df phase is triggered. Upon reducing the size difference still further at the same ideal pyrochlore nominal composition (cf. Fig. 4 with Fig. 3) the diffuse distribution in the df phase changes into "smoke rings" around $\frac{1}{2}[111]^*$ as a result of the fact that strain can apparently no longer be matched for alternate [111] metal ion planes.

If, instead of changing the Ln ion at the same nominal 50 mol% $LnO_{1.5}$ composition the composition is altered for the same Ln ion, then a pyrochlore to defect fluorite phase transition is again triggered when the effective cation size difference becomes too small (as a result of Zr^{4+} ions replacing Ln^{3+} ions or vice-versa; see, for example, the Ln = Sm portion of Fig. 2).

ACKNOWLEDGMENTS

One of us (Y.T.) gratefully acknowledges the support of an Australian Research Council (ARC) Post-Doctoral Fellowship. A significant component of this work was carried out while one of us (R.L.W.) was visiting the Departamento de Fisica de la Materia Condensada, Universidad del Pais Vasco, Bilbao, Spain as "Profesor Visitante Iberdrola." Iberdrola is gratefully acknowledged for financial support.

REFERENCES

1. A. Rouanet, *Rev. Int. Hautes Temp. Refract.* **8,** 161 (1971).
2. D. J. M. Bevan, W. W. Barker, T. C. Parks, and R. L. Martin, *in* "Rare Earth Research III" (L. Eyring, Ed.), p. 441. Gordon and Breach, New York, 1965.
3. R. Collongues, F. Queyroux, M. Perez y Jorba, and J.-C. Gilles, *Bull. Soc. Chim. France* **4,** 1141–1149 (1965).
4. S. García-Martin, M. A. Alario-Franco, D. P. Fagg, A. J. Feighery, and J. T. S. Irvine, *Chem. Mater.* **12,** 1729–1737 (2000).

5. Y. Tabira, R. L. Withers, J. Thompson, and S. Schmid, *J. Solid State Chem.* **142,** 393–399 (1999).
6. Y. Tabira and R. L. Withers, *J. Solid State Chem.* **148,** 205–214 (1999).
7. R. L. Withers, J. G. Thompson, P. J. Barlow, and J. C. Barry, *Aust. J. Chem.* **45,** 1375–1395 (1992).
8. R. E. Carter and W. L. Roth, *in* "Electromotive Force Measurements in High Temperature Systems" (C. B. Alcock, Ed.), Elsevier, New York, 1968.
9. T. H. Etsell and S. N. Flengas, *Chem. Rev.* **70,** 339–376 (1970).
10. K. J. de Vries, T. van Dijk, and A. J. Burgraaf, *in* "Fast Ion Transport in Solids" (Vashishta, Mundy, and Shenoy, Eds.). Elsevier, New York, 1979.
11. T. van Dijk, K. J. de Vries, and A. J. Burgraaf, *Phys. Status Solidi A* **58,** 115 (1980).
12. M. P. van Dijk, F. C. Mijlhoff, and A. J. Burgraaf, *J. Solid State Chem.* **62,** 377–385 (1986).
13. C. Heremans, B. J. Wuensch, J. K. Stalick, and E. Prince, *J. Solid State Chem.* **117,** 108–121 (1995).
14. D. Michel, M. Perez y Jorba, and R. Collongues, *Mater. Res. Bull.* **9,** 1457–1468 (1974).
15. J. G. Allpress and H. J. Rossell, *J. Solid State Chem.* **15,** 68–78 (1975).
16. B. Hudson and P. T. Moseley, *J. Solid State Chem.* **19,** 383–389 (1976).
17. H. J. Rossell and H. G. Scott, *J. Phys.* **C7,** C7-28 (1977).
18. M. Morinaga, J. B. Cohen, and J. Faber, *Acta Crystallogr. Sect. A: Found Crystallogr.* **36,** 520–530 (1980).
19. S. Suzuki, M. Tanaka, and M. Ishigame, *Jpn. J. Appl. Phys.* **24,** 401–410 (1985).
20. M. P. van Dijk, F. C. Mijlhoff, and A. J. Burggraaf, *J. Solid State Chem.* **62,** 377–385 (1986).
21. R. Neder, F. Frey, and H. Schultz, *Acta Crystallogr., Sect. A: Found Crystallogr.* **46,** 799 (1990).
22. R. L. Withers, J. G. Thompson, and P. J. Barlow, *J. Solid State Chem.* **94,** 89–105 (1991).
23. H. J. Rossell, J. R. Sellar, and I. J. Wilson, *Acta Crystallogr., Sect. B* **47,** 862 (1991).
24. R. Miida, M. Tanaka, H. Arashi, and M. Ishigame, *J. Appl. Crystallogr.* **27,** 67–73 (1994).
25. T. R. Welberry, B. D. Butler, J. G. Thompson, and R. L. Withers, *J. Solid State Chem.* **106,** 461–475 (1993).
26. T. R. Welberry, R. L. Withers, and S. C. Mayo, *J. Solid State Chem.* **115,** 43–54 (1995).
27. R. Miida, F. Sato, M. Tanaka, H. Naito, and H. Arashi, *J. Appl. Crystallogr.* **30,** 272–279 (1997).
28. T. R. Welberry, *Acta Crystallogr., Sect. A: Found Crystallogr.*, in press.
29. H. Nyman, S. Andersson, B. G. Hyde, and M. O'Keeffe, *J. Solid State Chem.* **26,** 123–131 (1978).
30. R. L. Withers, C. D. Ling, and S. Schmid, *Z. Kristallogr.* **214,** 296–304 (1999).
31. B. O. Loopstra and H. M. Rietveld, *Acta Crystallogr., Sect. B: Found Crystallogr.* **25,** 787 (1969).
32. R. D. Shannon, *Acta Crystallogr., Sect. A: Found Crystallogr.* **32,** 751–767 (1976).
33. N. Brese and M. O'Keeffe, *Acta Crystallogr., Sect. B* **47,** 192–197 (1991).